The Astrophysical Journal Letters, 973:L26 (13pp), 2024 September 20 https://doi.org/10.3847/2041-8213/ad72f1
© 2024. The Author(s). Published by the American Astronomical Society.
OPEN ACCESS

# Solar Wind Structures from the Gaussianity of Magnetic Magnitude

Zesen Huang (黄泽森)[1], Chen Shi (时辰)[1], Marco Velli[1], Nikos Sioulas[1], Olga Panasenco[2], Trevor Bowen[3], Lorenzo Matteini[4], Mingtao Xia (夏铭涛)[5], Xiaofei Shi (石晓霏)[1], Sheng Huang (黄胜)[6], Jia Huang (黄佳)[3], and Lizet Casillas[1]

[1] Department of Earth, Planetary, and Space Sciences, University of California, Los Angeles, CA, USA; zesenhuang@ucla.edu, cshi1993@ucla.edu, mvelli@ucla.edu
[2] Advanced Heliophysics, Pasadena, CA 91106, USA
[3] Space Sciences Laboratory, University of California, Berkeley, CA 94720-7450, USA
[4] Imperial College London, South Kensington Campus, London SW7 2AZ, UK
[5] Courant Institute of Mathematical Sciences, New York University, New York, NY 10012, USA
[6] Center for Space Physics, Boston University, Boston, MA, USA
*Received 2024 May 20; revised 2024 July 30; accepted 2024 August 12; published 2024 September 18*

## Abstract

The heliosphere is permeated with highly structured solar wind originating from the Sun. One of the primary science objectives of Parker Solar Probe (PSP) is to determine the structures and dynamics of the plasma and magnetic fields at the sources of the solar wind. However, establishing the connection between in situ measurements and structures and dynamics in the solar atmosphere is challenging: most of the magnetic footpoint mapping techniques have significant uncertainties in the source localization of a plasma parcel observed in situ, and the PSP plasma measurements suffer from a limited field of view. Therefore, it lacks a universal tool to self-contextualize the in situ measurements. Here we develop a novel time series visualization method named Gaussianity Scalogram. Utilizing this method, by analyzing the magnetic magnitude data from both PSP and Ulysses, we successfully identify in situ structures that are possible remnants of solar atmospheric and magnetic structures spanning more than 7 orders of magnitude, from years to seconds, including polar and midlatitude coronal holes, as well as structures compatible with supergranulation, "jetlets" and "picoflares." Furthermore, computer simulations of Alfvénic turbulence successfully reproduce the Gaussianization of magnetic magnitude, supporting the observed distribution. Building upon these discoveries, the Gaussianity Scalogram can help future studies to reveal the fractal-like fine structures in the solar wind time series from both PSP and a decades-old data archive.

*Unified Astronomy Thesaurus concepts:* Solar wind (1534); Solar physics (1476); Solar corona (1483); Interplanetary turbulence (830); Solar magnetic fields (1503)

*Materials only available in the online version of record: animation*

## 1. Introduction

The solar atmosphere is highly structured both spatially and temporally (S. D. Bale et al. 2019; J. C. Kasper et al. 2019). Recent studies have successfully established connections between Parker Solar Probe (PSP; N. J. Fox et al. 2016; see N. E. Raouafi et al. 2023a for a review of results of the first four years of the mission) in situ observations and solar atmospheric structures including midlatitude coronal holes (S. T. Badman et al. 2023; N. Davis et al. 2023), pseudostreamers (J. C. Kasper et al. 2021), and supergranulation (S. D. Bale et al. 2023, 2021; N. Fargette et al. 2021), even though alternative explanations remain (C. Shi et al. 2022). Recent advances in remote sensing provide strong support for the minutes-long small-scale jetting activity from magnetic reconnection ("jetlets") as a major source of the solar wind (N. E. Raouafi et al. 2023b). In addition, EUV observations from Solar Orbiter (D. Müller et al. 2020) unveiled the ubiquitous brightening termed "picoflare" (L. P. Chitta et al. 2023) with associated jets that last only a few tens of seconds, suggesting the solar wind source might be highly intermittent. However, magnetic footpoint mapping methods (S. T. Badman et al. 2020, 2023; O. Panasenco & M. Velli 2020) use photospheric magnetic field observations over the whole visible disk that are refreshed at best once every 6 hr and lack, of course, any real temporal reliability for the far side. Therefore, such methods are hardly able to reliably contextualize and explain the boundaries of the highly structured solar wind in situ time series, except perhaps in a statistical sense.

Using a data mining approach, this study starts by reporting an unexpected property of the solar wind. We find that when the magnetic magnitude $B$ is normalized by a power-law fit with regard to the heliocentric distance, it occasionally exhibits a perfect Gaussian distribution. Based on this discovery, we introduce a novel time series visualization method named Gaussianity Scalogram (GS) to visualize the scale-dependent Gaussianity of $B$. Applying this method to data from PSP and Ulysses, we successfully identified characteristics of in situ remnants of coronal holes (S. T. Badman et al. 2023; N. Davis et al. 2023) and switchback patches (C. Shi et al. 2022; S. D. Bale et al. 2023, 2021). Additionally, we discovered structures that are temporally compatible with small-scale jetting activities, including "jetlets" and "picoflares" (L. P. Chitta et al. 2023; N. E. Raouafi et al. 2023b). The rest of the Letter is structured as follows: In the next section, we describe the helioradial power-law fit and the construction of GS. In Section 3, we present some applications of GS. In Section 4, we discuss the computer simulation of Gaussianization of $B$ in MHD turbulence and the major implications. In Section 5, we conclude and summarize our results.

Original content from this work may be used under the terms of the Creative Commons Attribution 4.0 licence. Any further distribution of this work must maintain attribution to the author(s) and the title of the work, journal citation and DOI.

## 2. Helioradial Dependence of $B$ and the Gaussianity Scalogram

Two of the most interesting yet overlooked features of the time series of the solar wind magnetic field magnitude $B$ are that (1) sometimes $B$ displays a surprisingly stable power-law dependence on the heliocentric distance $R$ and (2) by applying a helioradial power-law fit between $B$ and $R$, i.e., $B \propto R^{-s}$, the fit normalized magnetic magnitude $B^* = B(R/R_0)^s$ sometimes displays a near-perfect Gaussian distribution. This is illustrated in Figures 1(a)–(c), where the selected interval is highlighted with a golden bar in panel (a) and the helioradial power-law fit (fit index $s = 1.86$) is shown in the inset figure. The histogram of $B$ is shown in blue in panel (b) and the normalized $B^*$ is shown in red. To illustrate the close proximity of the probability density function of $B^*$ ($\mathrm{PDF}_{B^*}$) to a Gaussian distribution ($\mathcal{N}$), a standard Gaussian curve is overplotted in panel (c) (shifted with the mean value $\langle B^* \rangle$ and scaled with the standard deviation $\sigma_{B^*}$). The Jensen–Shannon distance (JSD) of base $e$ (a statistical distance metric between probability density functions; J. Lin 1991) is calculated between $\mathrm{PDF}_{B^*}$ and $\mathcal{N}$, and the value is $\mathrm{JSD}(\mathrm{PDF}_{B^*}, \mathcal{N}) = 10^{-1.431}$, indicating considerable closeness between two distribution functions (for the benchmark, see Appendix A). In addition, this highly Gaussian $B^*$ interval coincides with the radial solar wind speed profile, which is visualized with radial colored lines in panel (a) and Figure 2(c) (compiled with SPAN-ion from SWEAP suite; J. C. Kasper et al. 2016). From November 17 to November 20, the spacecraft was immersed in the high-speed solar wind, indicating its coronal hole origin. The JSD produced by this process is represented as one pixel (tip of the green pyramid) in GS shown in panel (d3), and the scalogram for the corresponding helioradial power-law fit index $s$ is displayed in panel (d4).

Each pixel in the GS is characterized by a timestamp ($t_{\mathrm{mid}}$) and a window size (win), similar to a wavelet scalogram. Uniquely in GS, the step size in win (vertical axis) is chosen to be twice the step size in $t_{\mathrm{mid}}$ (horizontal axis), and thus the time range covered by one pixel corresponds to the same time range covered by three pixels in the following row, and so on toward the smallest scales. Therefore, if an interval and the nested subintervals possess similar characteristics (e.g., relatively small JSD regardless of $t_{\mathrm{mid}}$ and win within the interval), a pyramidal structure is expected from the GS, and the base of the pyramid indicates the start and end time of the interval. One example is highlighted by the green dashed pyramid in panel (d3), where the tip of the pyramid is in fact selected a posteriori as the local minimum in the GS ($\mathrm{PDF}_{B^*}$ being closest to Gaussian among the surrounding time and scales). Ample information can be inferred from the GS: (1) A semi-crossing of the heliospheric current sheet (HCS) at noon on November 22 is visualized as an inverted black pyramid. This is because the rapid drop of $B$ during HCS crossing can significantly destroy its Gaussianity; (2) It has been confirmed recently by S. T. Badman et al. (2023) that the solar wind can be traced back to a single midlatitude coronal hole from November 17 to the end of November 20, and from another coronal hole for the whole day of November 21 (see also S. D. Bale et al. 2023; S. T. Badman et al. 2020; O. Panasenco & M. Velli 2020). The coronal holes are naturally visualized here as two white pyramids (green and red dashed lines) separated by a dark region around mid-night on November 20; (3) The helioradial power-law fit index $s$ is unexpectedly stable regardless of locations and scales and systematically deviates from $R^{-2}$ ($s \simeq 1.87 \pm 0.02$; see also S. D. Bale et al. 2019).

The clear correspondence between the white pyramid and the coronal hole encourages us to predict intervals of solar wind originating from coronal holes with GS compiled from PSP data. Among the first 14 encounters (2018 November–2022 December), we only identified one more (for a total of two) long intervals (>3 days) characterized by high Gaussianity in $B^*$. A panoramic view of these two long intervals is shown in Figure 2. The newly found interval from the inbound of E12, shown in Figure 3 and Figure 2(d), is characterized by a 5 day long highly Gaussian $B^*$ time series. For illustration purposes, the green pyramid in Figure 3(d3) is selected as the deepest local minimum in GS for win > 3 days. The histogram of $B^*$ is remarkably concentrated (panel (b)) and aligns with Gaussian almost perfectly within four standard deviations (panel (c)). Similar to Figure 1(c), the non-Gaussian part of $\mathrm{PDF}_{B^*}$ has a systematic bias toward magnetic holes (weaker magnetic magnitudes, for recent studies using PSP data; see, e.g., L. Yu et al. 2021, 2022), and the helioradial power-law fit index scalogram also shows a systematic deviation from $s = 2$, similarly $s \simeq 1.87 \pm 0.02$. To validate this prediction, independent results from potential field source surface modeling are shown in Figure 4 (see O. Panasenco & M. Velli 2020 for more details), which indicates that the selected interval is indeed magnetically connected to a midlatitude coronal hole.

## 3. Fractal-like Gaussian Structures in the Solar Wind

To substantiate the applications of GS, here we demonstrate several examples that visualize the fractal-like Gaussian structures in the solar wind (due to the rapid movement of PSP around perihelia, the structures in the in situ time series can be categorized into two kinds: spatial, longitudinal structures traversed by PSP; temporal (radial), radial structures advected by the solar wind and/or propagation of Alfvén waves) based on the Taylor hypothesis (J. C. Perez et al. 2021). From the largest scales: Ulysses, years-long polar coronal hole (D. J. McComas et al. 2003), toward the smaller scales: hours-long switchback patches (S. D. Bale et al. 2023, 2021; N. Fargette et al. 2021; C. Shi et al. 2022); minutes-long structures compatible with "jetlets" (N. E. Raouafi et al. 2023b); and seconds-long structures compatible with "pico-flares" (L. P. Chitta et al. 2023).

Figure 5 shows the GS of the first Ulysses orbit, and the color bar in panel (b) is enhanced compared to Figure 1(d3) for illustration purposes. The solar latitude and wind speed profile in panel (a) indicate that the spacecraft was in southern and northern polar coronal holes in the whole year of 1994, and from 1995 to 1997 (see also D. J. McComas et al. 2003). The two large white pyramids in the GS clearly correspond to the two polar coronal holes. Notably, the boundary observed in panel (b) results from an artificial cutoff in the helioradial power-law fit, as shown in panel (c). The cutoff value is chosen to be $R_{\mathrm{max}}/R_{\mathrm{min}} = 1.5$, below which the spacecraft is considered stationary, and $B$ is not normalized to $B^*$ using the helioradial power-law fit prior to the calculation of Gaussianity. However, the Gaussianity is much weaker in the polar coronal holes compared to the midlatitude coronal holes observed by PSP at a much smaller heliocentric distance, and the histograms of magnetic magnitude show a much more significant fat tail toward the side of the magnetic hole (not shown here). This indicates that the Gaussianity of magnetic magnitudes

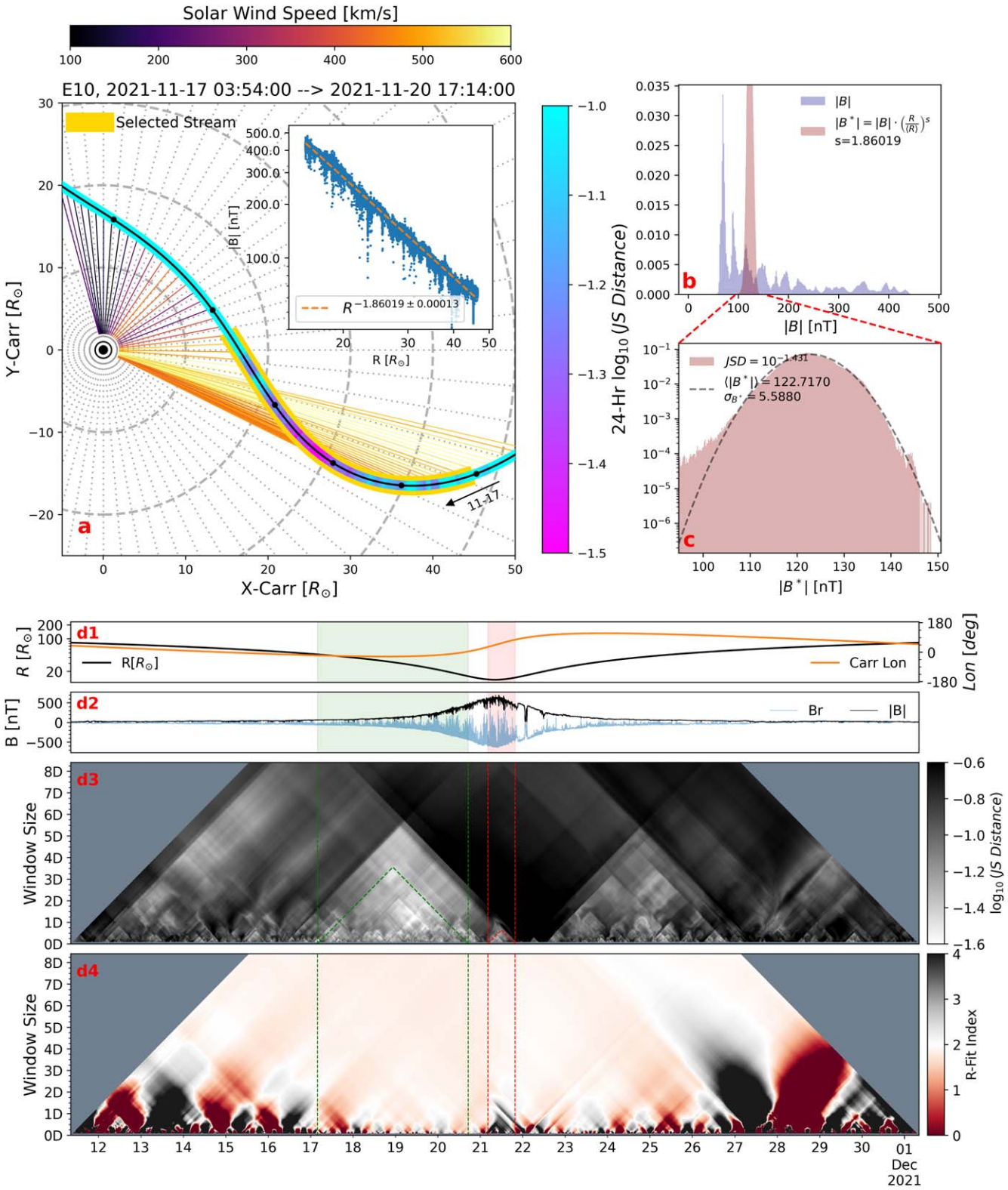



**Figure 1.** Selected interval from 2021 November, encounter 10 of PSP. (a) Spacecraft trajectory in the Carrington corotating frame from the afternoon of 2021 November 16 to the afternoon of 2021 November 22. Each day's start is indicated with black circles. The ballistic solar wind streamlines are plotted at a 2 hr cadence and colored according to the 10 minute averaged solar wind speed profile from SPAN-ion moment. The selected interval is emphasized with a golden bar, and the 24 hr window JSD of normalized magnetic magnitude $B^*$ is represented by the colored band. An inset displays the helioradial power-law dependence of $B$. (b) Histogram of $B$ and $B^*$ from the selected interval. (c) Histogram of $B^*$ and JSD(PDF$_{B^*}$). (d1) Spacecraft heliocentric distance (black) and Carrington longitude (orange). (d2) Magnetic field radial component $B_r$ and magnitude $B$. (d3) GS (scalogram of JSD). The selected interval is highlighted with the green pyramid. (d4) Helioradial power-law fit index scalogram of $B$.

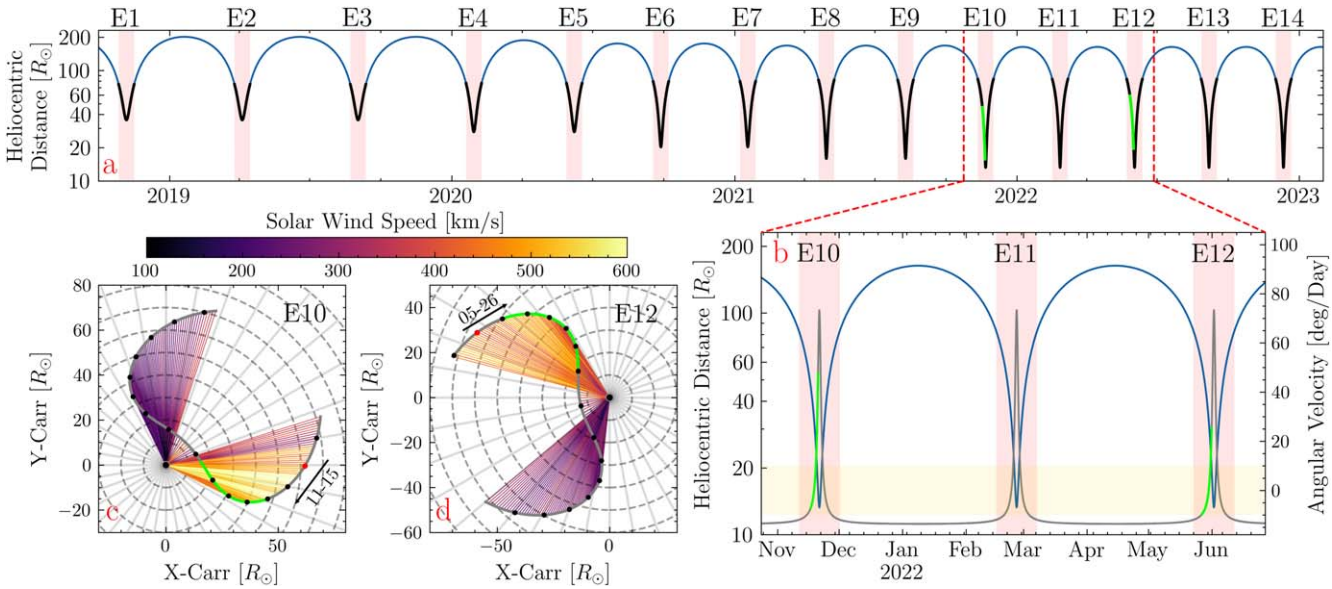



**Figure 2.** Panoramic plot of the data considered in this study. (a) Heliocentric distance of the spacecraft from encounter 1 to 14. The data analyzed in this study are from ±10 days around the perihelia, which are highlighted with black lines and pink-shaded areas. The two normally distributed long intervals under investigation are represented by the two green segments. (b) Detailed illustration of E10 to E12, with the spacecraft's angular velocity in the Carrington corotation frame displayed on the twin axis. The corotating periods ($\omega < 10$ [deg Day$^{-1}$]) are marked with golden-shaded areas, and the selected intervals are highlighted in green on top of the angular velocity profile. (c),(d) Synopsis plot of E10 and E12 spacecraft trajectories from ±8 days around the perihelion in the Carrington corotating frame. The starts of each day are indicated by black dots, and the two arrows show the spacecraft's entering directions, with the corresponding dates highlighted by red circles. The solar wind streamlines are colored according to the 10 minute averaged solar wind speed and are plotted every 2 hr. The two selected intervals are also highlighted in green.

decreases with increasing heliocentric distance, possibly due to the transition from low-$\beta$ to high-$\beta$ environment ($\beta = 2\mu_0 P/B^2$ is the ratio between plasma thermal pressure $P$ and magnetic pressure $B^2/2\mu_0$), and the plasma thermal pressure hence has a larger influence on the distribution of $B$. Additionally, this also indicates that magnetic holes are much more preferred than spikes in the solar wind plasma.

Figure 6 shows the hours-long switchback patches from a single midlatitude coronal hole in PSP E10, which have been recently proposed to be the remnants of the supergranulations in the solar atmosphere (S. D. Bale et al. 2023, 2021; N. Fargette et al. 2021). To indicate the spacecraft movement, the Carrington longitude of PSP is plotted every one degree on the top bars of both panels (a) and (b), and the color indicates spacecraft angular velocity in the corotating frame (blue: prograde, red: retrograde; see also Figure 1 for PSP trajectory in the corotating frame at the same perihelion). The magnetic magnitude is normalized with a universal helioradial power-law fit index ($s = 1.87$) and the GS is compiled with the high-resolution fluxgate magnetic data (∼292 Hz; see S. D. Bale et al. 2016; T. A. Bowen et al. 2020). The red dashed pyramids in panels (a) and (b) are drawn to highlight the $B^*$ intervals with a high level of Gaussianity. The selected intervals in panel (a) show that the GS effectively captures some of the switchback patches. When these are compared with the Carrington longitude, it becomes evident that some of the structures align with the size of supergranulation, as discussed in S. D. Bale et al. (2023). However, other structures, which are smaller in angular size and likely temporal in nature, could be more accurately attributed to the "breathing" phenomenon of the solar wind, as explained in T. Berger et al. (2017) and C. Shi et al. (2022). After the "fast radial scan" phase on November 18, the spacecraft began to rapidly retrograde on November 19 and November 20 (see Figure 1(a) for the spacecraft trajectory in the corotating frame). For better comparison, an expanded view is shown in panel (b). The second and third pyramids also show decent capability of capturing the switchback patches, whereas the first pyramid seems to capture a boundary between the patches. Starting from 7:00 on November 20, the remaining patches consistently exhibit a high level of Gaussianity across all scales and locations, resulting in indistinct boundaries between them.

Figure 7 presents a hierarchic GS of the midlatitude coronal hole from the inbound of PSP E12. In panels (d) and (e), focusing on the smallest scales resolvable by the JSD (approximately 1 minute, corresponding to around 20,000 data points for the shortest interval; for details on how the number of data points influences this analysis, see the Appendix), we observe a surprising number of structures with distinct boundaries. In fact, these structures, typically lasting 1–10 minutes, are omnipresent in the Alfvénic solar wind for all PSP encounters. Notably, they are not limited to winds with a clear coronal hole origin, such as those in the outbound paths of E12 (for more details, see the video in the supplementary materials). These structures are typically separated (interrupted) by radial jets (i.e., individual switchbacks), and these separations are frequently accompanied by close to kinetic-scale ($\lesssim$5 s) fluctuations that are bursty and short-lived in all three components of the magnetic field. For further illustration, refer to the skewness scalogram video in the supplementary materials. Unlike the spatial structures shown in panels (a), (b), and (c) (as well as in Figures 1 and 5), the longitude change of the spacecraft for each structure in panels (d) and (e) is less than $0.^\circ1$, as indicated by the crosses plotted every 0.1 Carrington longitude in the top bar. Therefore, these structures are likely temporal, i.e., advected by the solar wind. All of these features are highly compatible with the "jetlets" observed in equatorial coronal holes (N. E. Raouafi et al. 2023b), and therefore could potentially be the "building blocks" of the solar wind. In fact, even finer structures can be found with the normalized standard deviation ($\sigma_{B^*}/\langle B^* \rangle$) scalogram and skewness scalogram shown

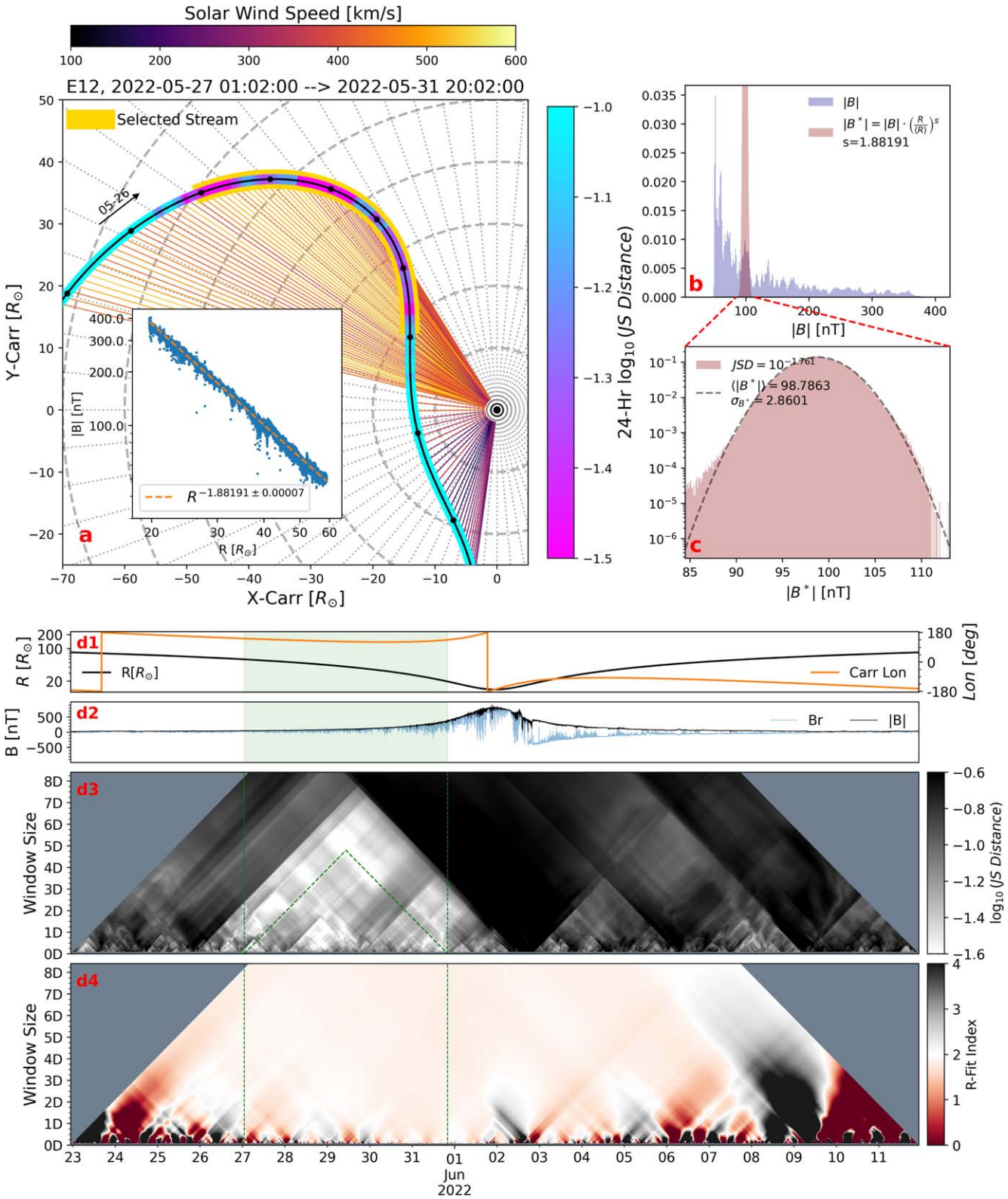



**Figure 3.** Selected interval from E12.

in Figure 8. For example, the small white pyramid around 8:36 in Figure 7(e) has two 30 s long substructures nested beneath in Figure 8. These seconds-long structures are intervals with smaller standard deviations compared to the surroundings, and their interruptions are temporally compatible with the "picoflare" (L. P. Chitta et al. 2023).

## 4. Discussion

These observations indicate that the Alfvénic solar wind is permeated with highly Gaussian magnetic magnitude intervals that are often interrupted by radial jets (switchbacks) every 1–10 minutes. In addition, the magnetic fluctuations inside the

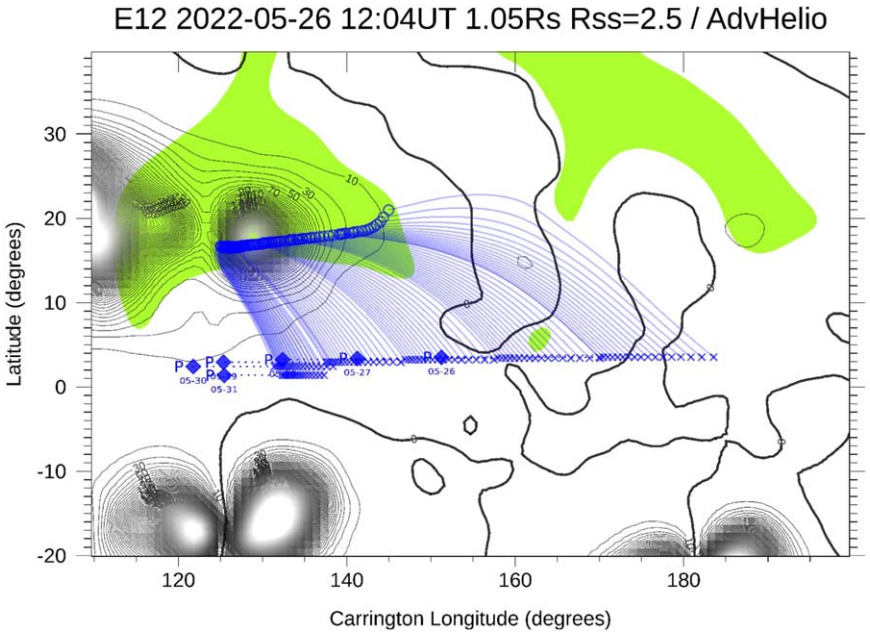



**Figure 4.** Magnetic field connectivity with the solar sources during inbound of PSP encounter 12. The thick black lines are the model neutral lines. Black contours indicate magnetic field pressure at 1.05 $R_s$. The ballistic projection of the PSP trajectory (blue diamonds) on the source surface (blue crosses) and down to the solar wind source regions (blue circles) is calculated for source surfaces $R_{ss}/R_s = 2.5$ (see O. Panasenco & M. Velli 2020 for details) and measured in situ solar wind speed ±80 km s1. Open magnetic field regions are shown in blue (negative) and green (positive).

intervals often resemble the small-amplitude outward-propagating linear Alfvén waves. It is therefore reasonable to model the system using small-amplitude Alfvénic MHD turbulence. Figure 9 shows the temporal evolution of the JSD(PDF$_B$, $\mathcal{N}$) of a 3D MHD small-amplitude Alfvénic turbulence simulation (C. Shi et al. 2023). The simulation is run with a $512^3$ periodic box and is initialized with unidirectional small-amplitude linearly polarized Alfvén waves with isotropic wavevector spectrum (see the Methods section for more details). At $t = 0.00\,t_A$ (Alfvén crossing time $t_A = L/v_A$, where $L$ is the simulation box size), the point-spread function (PDF) PDF$_B$ deviates significantly from a Gaussian distribution due to the small-amplitude shear Alfvén wave initialization (fluctuations in $B$ are positive definite). The corresponding JSD is highlighted as the first red dot in the lower panel and is much larger than 0. Surprisingly, within one Alfvén crossing time at $t = 0.40\,t_A$, the distribution of $B$ rapidly relaxes to a near-perfect Gaussian distribution, and the JSD rapidly drops toward the ground-truth value (see Benchmark in Methods). As the simulation evolves, the JSD remains considerably small, and thus the distribution of $B$ remains very close to Gaussian. The simulation indicates that Gaussian is the natural relaxation state for magnetic magnitude in small-amplitude Alfvénic turbulence, consistent with the ubiquitous 1–10 minutes Gaussian intervals found in the solar wind. However, a 3D analytical model of a switchback with constant magnetic magnitude and fully open field lines is not yet available (see A. Tenerani et al. 2020; L. Matteini et al. 2024; C. Shi et al. 2024b; J. Squire & A. Mallet 2022 for recent progress on switchback modeling). Therefore, our simulation cannot reproduce the realistic physical condition of the solar wind turbulence in which large-amplitude spherically polarized Alfvénic fluctuations dominate.

Nevertheless, the simulation suggests that information is fully exchanged within the system, as it propagates at Alfvén speed throughout the simulation box. This allows $B$ to relax to a Gaussian distribution, which occurs within about 0.5 $t_A$, i.e., the time it takes for Alfvén waves to carry information from the center of the simulation box to its edges. However, in observations, it is not reasonable to assume that the information is fully exchanged for the hours-, days-, or even months-long structures shown in Figures 1, 5, and 6, due to the super-Alfvénic nature of the solar wind close to the Sun and the longitudinal movement of the spacecraft. Beyond the Alfvén surface (J. C. Kasper et al. 2021), the information can only propagate radially outwards in the solar wind. Moreover, the structures that last an hour or longer are likely spread spatially and longitudinally. However, Alfvén waves, along with the information they carry, are guided by the background magnetic field, which predominantly points radially outwards around PSP perihelia. Therefore, alternative explanations are necessary for the observed hours-long (and longer) Gaussian structures. The simplest explanation for the Gaussian $B$ structures originating from coronal holes (midlatitude coronal holes from E10 and E12, and polar coronal holes from Ulysses) is the pressure balance between the open coronal field lines. Close to the Sun, the solar wind originating from the coronal holes is mostly magnetic dominant (plasma $\beta = 2\mu_0 P/B^2 \ll 1$, see e.g., J. C. Kasper et al. 2021). Therefore, to maintain pressure balance, the open field lines from the same coronal hole tend to evolve to a state in which the magnetic pressure $P_B = B^2/2\mu_0$ is mostly uniform for a given cross section of the magnetic flux tube. In Figure 1, the helioradial power-law normalization of $B$ essentially maps the magnetic field line density, which is effectively the magnetic flux density due to the spherical polarization of the Alfvén waves, from various radial distances and transverse locations to a single cross section of the flux tube (for more details of spherical polarization of Alfvén waves, see the appendix and L. Matteini et al. (2014, 2015)). As a support of this idea, from the PSP observations of E10 and E12 (Figures 1 and 3), the helioradial power-law normalization of $B$ effectively collapses the histogram of $B$ into a delta-

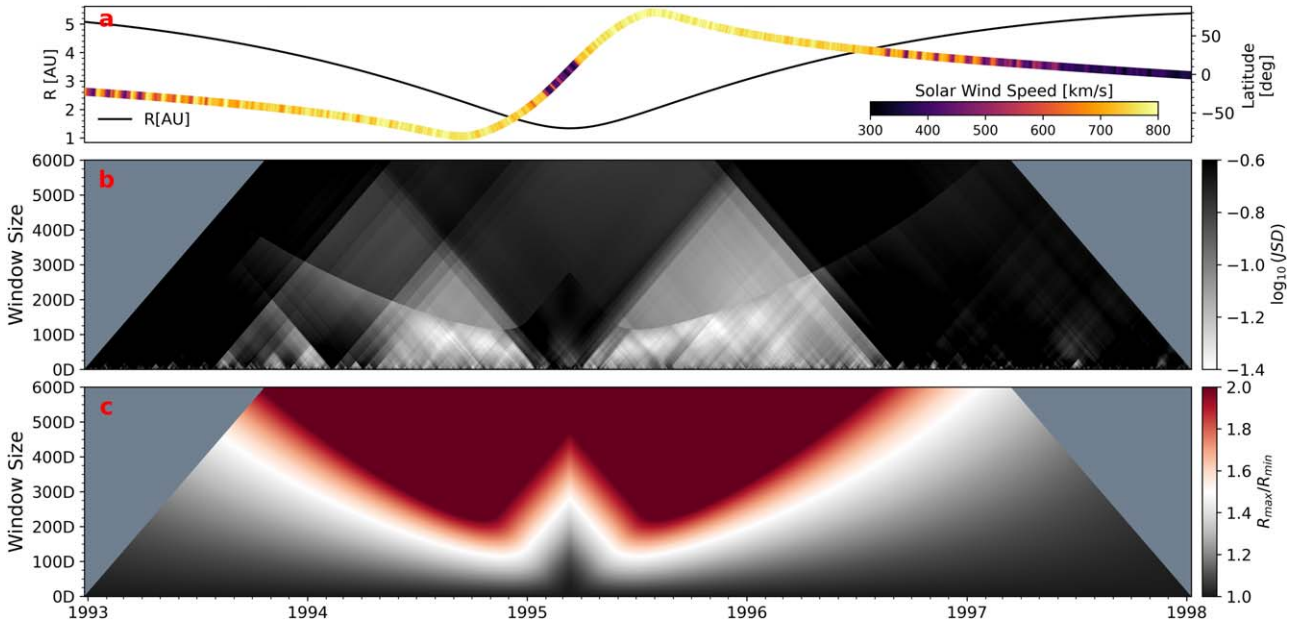



**Figure 5.** Gaussianity Scalogram from Ulysses' first orbit from 1993 to 1998. (a) Ulysses heliocentric distance $R$ (black line) and heliographic latitude colored with local 48 hr averaged solar wind speed. (b) GS compiled from magnetic magnitude $B$ (lower half) and helioradial power-law normalized magnitude $B^*$ (upper half). (c)$R_{\max}/R_{\min}$ of each interval (pixel), where the cutoff value is chosen to be $R_{\max}/R_{\min} = 1.5$, beyond which $B$ is normalized into $B^*$ using the helioradial power-law fit before calculating the Gaussianity.

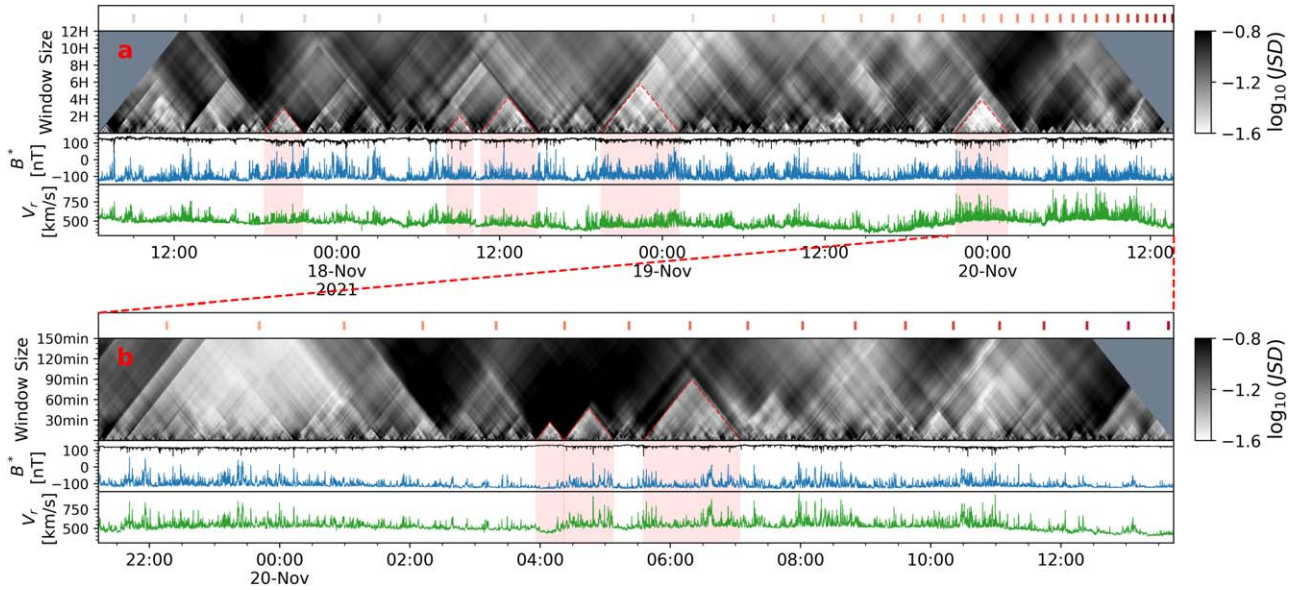



**Figure 6.** GS of the PSP E10 inbound midlatitude coronal hole. (a) From top to bottom: Carrington longitude plotted with 1° cadence colored with spacecraft angular velocity in the corotating frame (blue: prograde, red: retrograde); JS scalogram with 1 minute resolution, normalized magnetic magnitude $B^*$, radial component $B_r^*$, and radial solar wind speed $V_r$; (b) expanded view of panel (a) with a 10 s resolution.

function-like histogram of $B^*$. This is indicative of identical field line density within a single coronal hole due to the magnetic pressure balance. The detailed distribution of $B^*$ is hence the feature of the noise in magnetic magnitude within a single coronal hole, which can be considered as a 1D random walk (continuous addition of small-amplitude random fluctuations that can be considered as samples drawn from the same stochastic source throughout its passage from the base of the corona to the spacecraft). Therefore, the Gaussian distribution of $B^*$ can be easily explained as the result of the stopped random walk according to the central limit theorem. Nevertheless, difficulties remain with the physical origin of hours-long structures. They may be the manifestation of the denser field line density originating from a single supergranule based on its connection with switchback patches, but a more detailed discussion lies beyond the scope of this study.

Finally, the existence of a stable power-law dependence of $B$ with regard to heliocentric distance $R$ itself already sheds light on the physics of the solar wind originating from coronal holes. As solar activities ramp up for solar cycle 25, four out of the five recent encounters (E10, E11, E12, E14) of PSP show a systematic preference for a single helioradial power-law index,

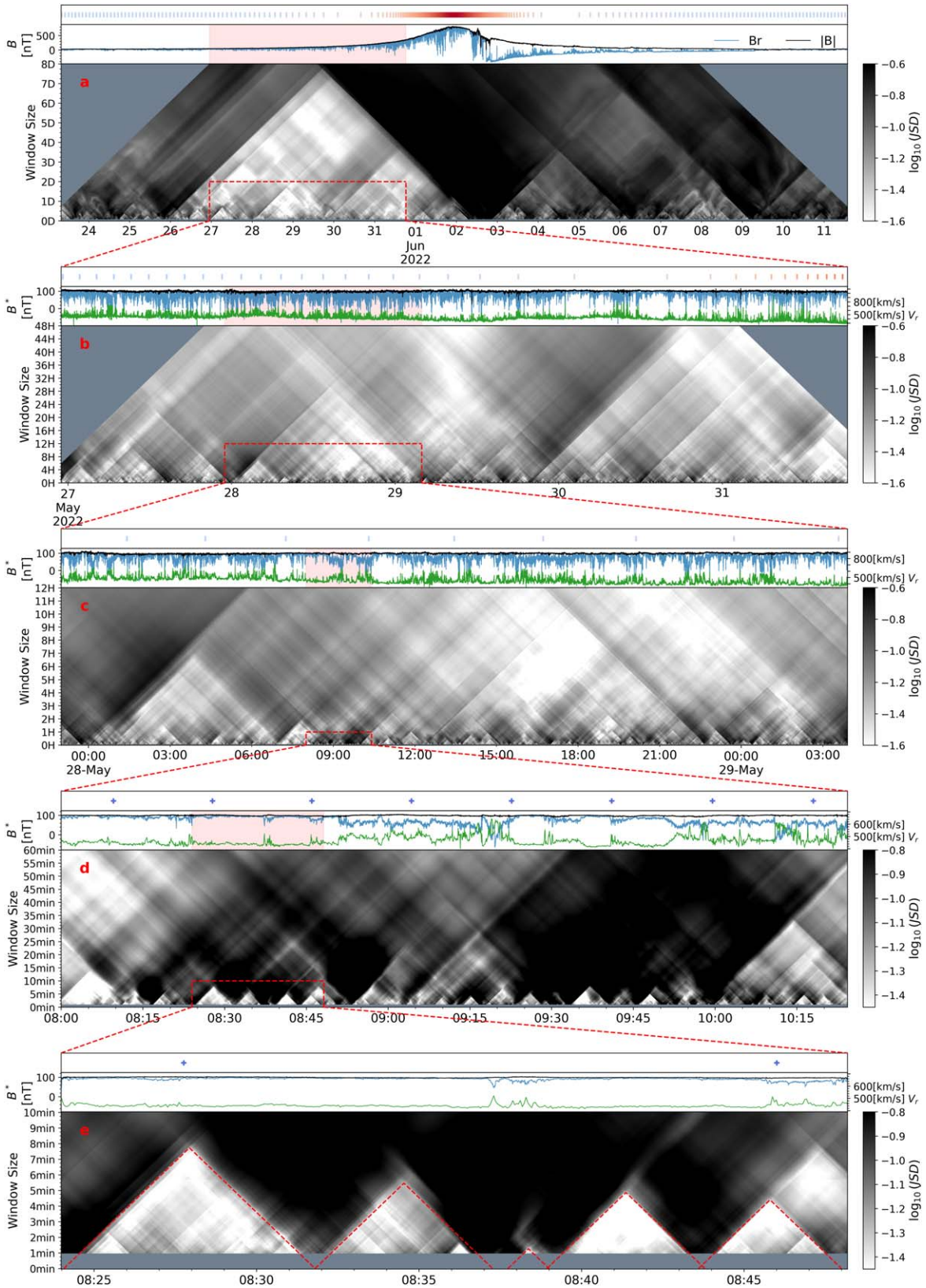



**Figure 7.** Hierarchic multiscale GS illustration of the midlatitude coronal hole from the PSP encounter 12 inbounds. For all subplots, the Carrington longitude of the spacecraft is shown in the top panel. For subplots (a) to (c), the bars are plotted every 1°, with colors indicating the heliocentric angular velocity in the solar corotating frame (blue: progradation, red: retrogradation). For subplots (d) and (e), the crosses are plotted every 0°.1. The corresponding magnetic field magnitude $B$ and radial component $B_r$ are shown in the second panel of each subplot; and except for subplot (a), the magnetic field is normalized with helioradial power-law fit. The radial solar wind speed $V_r$ is also shown in subplots (b)–(e). The animation shows the GS of the whole PSP E12. For completeness, the scalogram of skewness of $B$ is also shown as the last panel in the animation.

(An animation of this figure is available in the online article.)

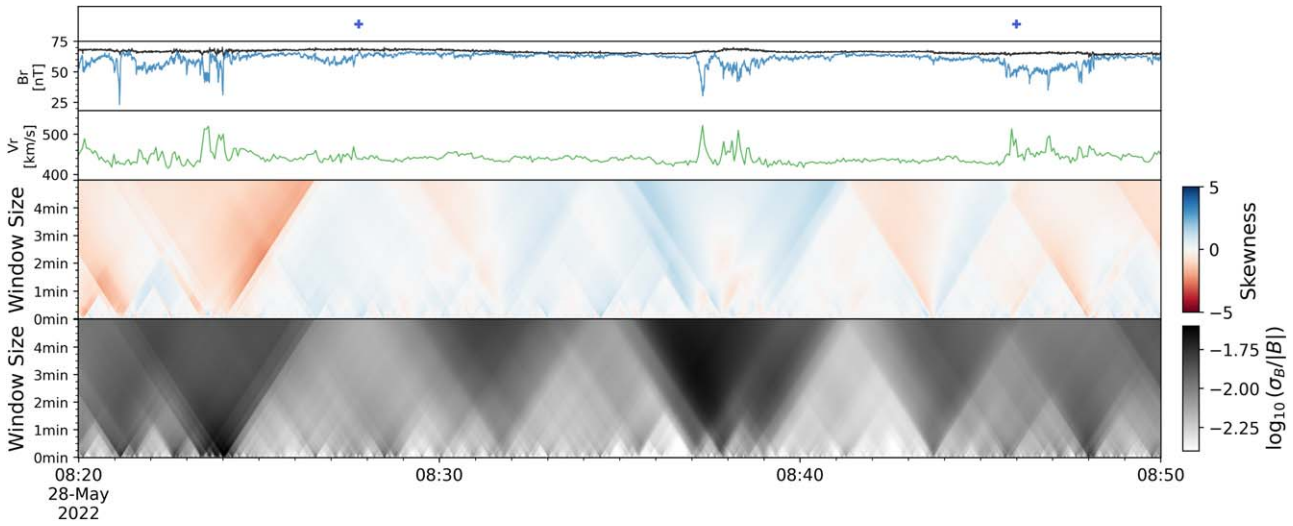



**Figure 8.** Skewness and normalized standard deviation scalogram. From top to bottom: spacecraft Carrington longitude plotted with 0.°1 cadence; magnetic magnitude ($B$, black) and radial component ($B_r$, blue); radial solar wind speed ($V_r$); skewness scalogram of $B$; normalized standard deviation scalogram of $B$.

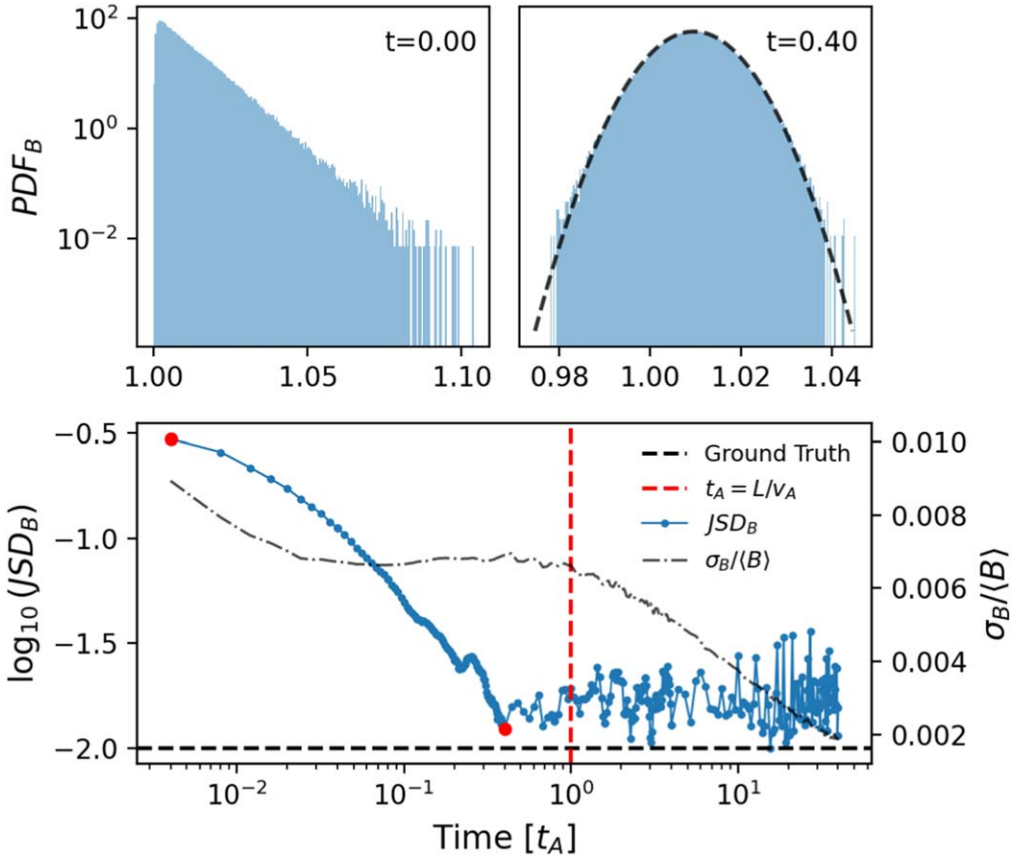



**Figure 9.** Relaxation of magnetic magnitude $B$ in Alfvénic MHD turbulence simulation. Upper panels: (Left) Probability distribution of $B$ ($\mathrm{PDF}_B$) at $t = 0.00\ t_\mathrm{A}$, where $t_\mathrm{A} = L/v_\mathrm{A}$ is the Alfvén time and $L$ is the size of the simulation box, $v_\mathrm{A}$ is the Alfvén speed; (Right) $\mathrm{PDF}_B$ at $t = 0.40\ t_\mathrm{A}$. Lower panel: time evolution of the JSD between $\mathrm{PDF}_B$ and GS (blue line), and normalized standard deviation of $B$ (dashed–dotted line). The time axis is normalized with the Alfvén time $t_\mathrm{A}$. The simulation time step of the upper left and right panels is highlighted with two red circles in the lower panel.

which consistently deviates from $R^{-2}$. However, the $R^{-2}$ power law, expected only from the dominant radial component $B_r$ as a result of the Parker spiral (conservation of magnetic flux in spherical expansion), is not strictly applicable to $B$, especially for PSP, due to the ubiquitous switchbacks. Due to the relation between $B$ and the local magnetic flux density, this is indicative of a stable expansion rate for the magnetic flux tube in the magnetic dominant wind ($\beta \ll 1$) close to the Sun. Such an expansion rate is crucial for the estimation of the WKB evolution of the fluctuation quantities like the magnetic and velocity field (Z. Huang et al. 2022; M. Velli et al. 1991; J. V. Hollweg 1973; M. Heinemann & S. Olbert 1980). It

should be noted that the fit indices of $B$ coincide with the helioradial dependence of the electron density compiled from quasi-thermal noise (O. Kruparova et al. 2023; M. Moncuquet et al. 2020), indicating that the deviation from $R^{-2}$ could be the evidence of active acceleration of the solar wind.

## 5. Conclusion and Summary

Compiled from the almost featureless magnetic magnitude time series from the solar wind, the GS unveils a striking number of fractal-like magnetic structures spanning over 7 orders of magnitude in time. These structures include spatial structures like polar coronal holes (D. J. McComas et al. 2003), midlatitude coronal holes (S. T. Badman et al. 2023), and switchback patches (S. D. Bale et al. 2023). They also include temporal structures compatible with "jetlets" (N. E. Raouafi et al. 2023b) and "picoflares" (L. P. Chitta et al. 2023), which are often interrupted by the radial jets (switchbacks). In addition, 3D MHD simulations have shown that Gaussian is the natural relaxation state for small-amplitude unidirectional Alfvénic turbulence. Minutes-long structures are hence likely to be the natural products of Alfvénic MHD turbulence. Thus, it is now clear that the Alfvénic solar wind is permeated with these intermittent Gaussian $B$ structures, which are self-similarly organized from seconds to years, and are possibly the remnants of the magnetic structures on the solar surface (M. J. Aschwanden et al. 2016; S. D. Bale et al. 2023; L. P. Chitta et al. 2023; N. E. Raouafi et al. 2023b; M. Aschwanden 2011; V. M. Uritsky & J. M. Davila 2012). This Letter reveals just a fraction of the rich structures uncovered by the GS from the solar wind time series. The GS proves to be a versatile tool, essential not only for deciphering the structure and dynamics of plasma and magnetic fields, one of the key objectives of the PSP mission (N. J. Fox et al. 2016), but also for revitalizing decades-old solar wind data from missions like Helios, Ulysses, and WIND. These efforts unveil new physics previously hidden within these data sets. Additionally, the GS applicability may extend beyond solar wind analysis, potentially serving other kinds of high-resolution stochastic time series data.

## Acknowledgments

Z.H. thanks Jiace Sun, Benjamin Chandran, Anna Tenerani, and Victor Réville for valuable discussions. C.S. is supported by NSF SHINE No. 2229566. C.S. acknowledges the support of Extreme Science and Engineering Discovery Environment (XSEDE) EXPANSE at SDSC through allocation No. TG-AST200031, which is funded by National Science Foundation grant No. ACI-1548562 (J. Towns et al. 2014). C.S. also acknowledges the support of Derecho: HPE Cray EX System (https://doi.org/10.5065/qx9a-pg09) of Computational and Information Systems Laboratory (CISL), National Center for Atmospheric Research (NCAR; allocation No. UCLA0063). This research was funded in part by the FIELDS experiment on the Parker Solar Probe spacecraft, designed and developed under NASA contract UCB No. 00010350/NASA NNN06AA01C, and the NASA Parker Solar Probe Observatory Scientist grant NASA NNX15AF34G, and NASA HTMS 80NSSC20K1275. M.V. acknowledges support from ISSI via the J. Geiss fellowship.

## Data Availability

The PSP and Ulysses mission data used in this study are openly available at the NASA Space Physics Data Facility (https://nssdc.gsfc.nasa.gov) and were analyzed using the following open-source software: `NumPy` (C. R. Harris et al. 2020), `SciPy` (P. Virtanen et al. 2020), `Matplotlib`, `SPEDAS` (V. Angelopoulos et al. 2019), `Numba` (S. K. Lam et al. 2015).

## Appendix A
## Jensen–Shannon Distance, Gaussianity Scalogram, and Benchmark

The JSD is the square root of the Jensen–Shannon divergence (J. Lin 1991), which is the symmetrized and smoothed version of the Kullback–Leibler divergence (S. Kullback & R. A. Leibler 1951). Due to its symmetry and smoothness, JSD is an ideal metric for the similarity between the observed magnetic magnitude distribution and the Gaussian distribution. For two discrete probability distribution functions $P$ and $Q$ defined in the same space $\mathcal{X}$, the Jensen–Shannon divergence is calculated as follows:

$$\mathrm{JSD}(P\|Q) = \frac{1}{2}D_{\mathrm{KL}}(P\|M) + \frac{1}{2}D_{\mathrm{KL}}(Q\|M), \tag{A1}$$

where $M = (P+Q)/2$ is the mixture distribution of $P$ and $Q$, and $D_{\mathrm{KL}}(P\|Q)$ is the Kullback–Leibler divergence:

$$D_{\mathrm{KL}}(P\|Q) = \sum_{x\in\mathcal{X}} P(x)\log\left(\frac{P(x)}{Q(x)}\right). \tag{A2}$$

In this study, we use `scipy.spatial.distance.jensenshannon` (P. Virtanen et al. 2020) to calculate the JSD. This program uses the natural base logarithm in the Kullback–Leibler divergence, and therefore the final JSD is bounded by $[0, \sqrt{ln(2)}]$.

The GS is a map where the vertical axis is window size (win) and the horizontal axis is the central time of each interval ($t_{\mathrm{mid}}$), together forming a scalogram of the JSD between the normalized probability density function of a given interval PDF($t_{\mathrm{mid}}$, win) and the standard Gaussian distribution $\mathcal{N}(0, 1)$, i.e., JSD(PDF($t_{\mathrm{mid}}$, win), $\mathcal{N}(0, 1)$), or simply JSD(PDF, $\mathcal{N}$). To calculate PDF($t_{\mathrm{mid}}$, win) from the ensemble of samples from a given interval, there are three controlling parameters: sample size $N_p$, number of bins $N_b$, and number of standard deviations considered $\sigma$. In addition, for benchmark purposes, it is necessary to calculate the JSD between some well-known symmetric distributions and the standard Gaussian distribution. The summary of the influence of the controlling parameters and the comparison with well-known distributions are shown in Figure A1.

The JSD between Laplace and logistic distributions and a Gaussian distribution as a function of the standard deviation range considered is shown in panel (a). The JSD value stabilizes approximately at $5\sigma$, and therefore for all GS shown in this Letter, the PDFs are all compiled for $\pm 5\sigma$. To see how $N_p$ and $N_b$ control the JSD value, samples are repeatedly drawn from a true logistic distribution to calculate JSD(Logistic, $\mathcal{N}|N_p, N_b$). In panel (c), we see a much more stabilized region for large enough $N_p$ and not-too-large $N_b$ (the stable region is orange-ish because the theoretical value at $5\sigma$ is slightly smaller than the true value shown in panel (a) as the dark red horizontal dashed

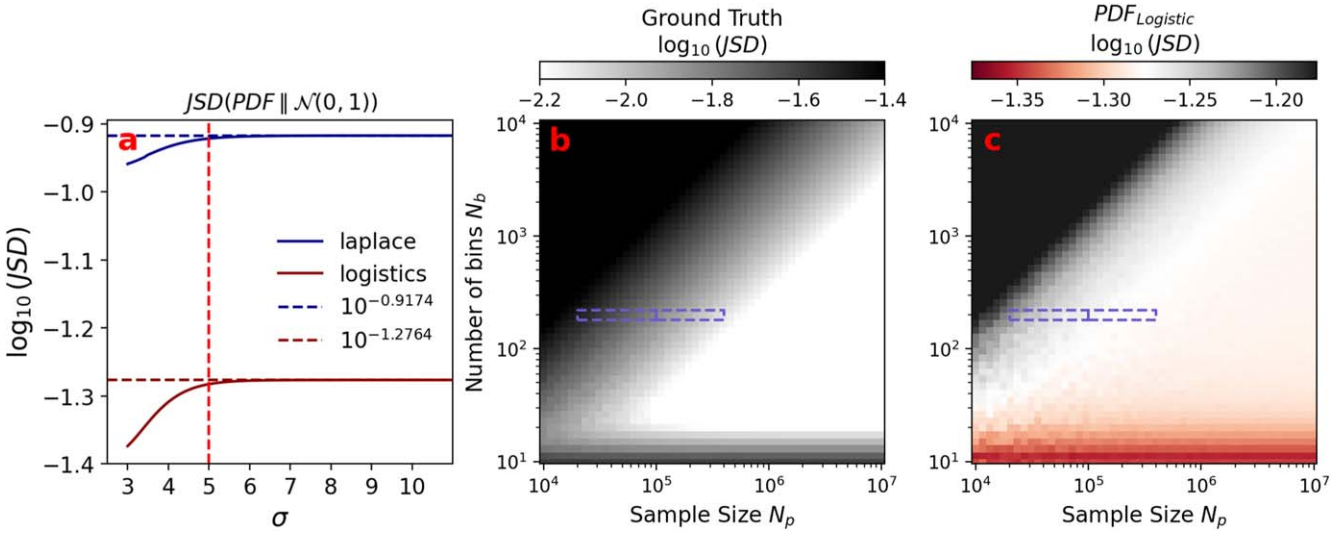



**Figure A1.** Benchmark of all three free parameters: number of standard deviation $\sigma$, number of bins, and number of points. (a) JSD between a given probability distribution function and the standard Gaussian distribution $\mathcal{N}(0, 1)$. (b) "Ground-truth" values, i.e., the JSD of the histogram with $N_b$ number of bins estimated from $N_p$ number of points from $\mathcal{N}(0, 1)$. (c) The same $x$- and $y$-bins as panel (b), with values of $\mathrm{JSD}(\mathrm{PDF}_{\mathrm{Logistic}} \| \mathcal{N}(0, 1))$.

line). Two purple dashed regions are highlighted in panel (c), where the right one indicates the parameter space used for low-resolution GS shown in Figures 1 and 3, and the left one corresponds to the high-resolution version shown in Figures 7(c)–(e).

In addition, $N_p$ and $N_b$ also influence the ground-truth value, i.e., the JSD between an ensemble statistically drawn from a Gaussian generator and the real Gaussian PDF, which is not available in closed form (F. Nielsen 2019). To obtain the ground-truth value, the PDF is a histogram of equally spaced $N_b$ bins located within $\pm 5\sigma$ compiled from $N_p$ independent samples drawn from a standard Gaussian source `numpy.random.randn` (C. R. Harris et al. 2020), and then the JSD is the averaged distance between the statistically calculated PDF($N_p$, $N_b$) (repeated 30 times for each $N_p$ and $N_b$) and the true Gaussian PDF. The standard deviation is found to be small for a given tuple of $N_p$ and $N_b$. The resulting $N_p$–$N_b$ map is shown in panel (b), and the two-parameter space considered is also shown as the purple dashed region. Even for the poorest case ($N_p \sim 20000$), the ground-truth value is still sufficiently away from JSD(Logistic, $\mathcal{N}$).

## Appendix B
## Spherical Polarization of Alfvén Waves

Although the spherical (arc) polarization of observed Alfvén waves is well-known (B. T. Tsurutani et al. 1994; X. Wang et al. 2012; Z. Johnston et al. 2022; P. Riley et al. 1996; J. V. Hollweg 1974; B. J. Vasquez & J. V. Hollweg 1996; L. Del Zanna 2001; D. V. Erofeev 2019; J. Squire & A. Mallet 2022), we provide here a description here for spherically polarized Alfvén waves in a magnetically dominated plasma (plasma $\beta = 2\mu_0 P/B^2 \lesssim 0.1$, typical for Alfvénic solar wind measured by PSP around perihelion J. C. Kasper et al. 2021). Similar to L. Matteini et al. (2014), this considers the background magnetic field $\boldsymbol{B}_0$ to have the same constant magnetic magnitude $B$, differently from J. V. Hollweg (1974), where $\boldsymbol{B}_0$ is calculated as the spatial average $\langle \boldsymbol{B} \rangle$, yielding a smaller field magnitude than the radius of the sphere $B$.

For a fluctuation-free magnetic flux tube originating from a coronal hole, the magnetic field is pointing mostly radially in the high corona and solar wind close to the Sun. The spherically polarized Alfvén waves can therefore be considered as a perturbation to this otherwise quiet system. To maintain the constant $B$ state observed in the solar wind, the additive magnetic perturbation has to "switch back" on top of the radial background field. This scenario is depicted in Figure 4 in L. Matteini et al. (2014). The constant magnetic magnitude $B$ is shown as the radius of the circle and the static radial field from the coronal hole is $\boldsymbol{B}_0$. To maintain the constant $B$ state, the perturbation to the system $\boldsymbol{B}_1$ is restricted to the semicircle, and the resultant magnetic vector $\boldsymbol{B} = \boldsymbol{B}_0 + \boldsymbol{B}_1$ can thus fluctuate on a constant sphere of $B$. Following this setup, the magnetically dominant ($p \ll B^2/2\mu_0$) incompressible MHD equations can be rewritten as follows ($\rho = \mathrm{const}$, $p = \mathrm{const}$, $B^2 = \mathrm{const}$, $\boldsymbol{B} = \boldsymbol{B}_0 + \boldsymbol{B}_1$):

$$\frac{\partial \boldsymbol{u}}{\partial t} = \boldsymbol{b} \cdot \nabla \boldsymbol{b} - \boldsymbol{u} \cdot \nabla \boldsymbol{u}, \tag{B1}$$

$$\frac{\partial \boldsymbol{b}}{\partial t} = \boldsymbol{b} \cdot \nabla \boldsymbol{u} - \boldsymbol{u} \cdot \nabla \boldsymbol{b}, \tag{B2}$$

where $\boldsymbol{b} = \boldsymbol{B}/\sqrt{\mu_0 \rho} = \boldsymbol{B}_0/\sqrt{\mu_0 \rho} + \boldsymbol{B}_1/\sqrt{\mu_0 \rho} = \boldsymbol{b}_0 + \boldsymbol{b}_1$. Assuming the frame is comoving with the bulk flow and the perturbations are Alfvénic, i.e., $\boldsymbol{u} = \boldsymbol{u}_1$ and $\boldsymbol{u}_1 = \pm \boldsymbol{b}_1$, the equations can be further reduced into a wave equation:

$$\frac{\partial^2 \boldsymbol{b}_1}{\partial t^2} = (\boldsymbol{v}_a \cdot \nabla)^2 \boldsymbol{b}_1, \tag{B3}$$

where $\boldsymbol{v}_a = \boldsymbol{b}_0 = \boldsymbol{B}_0/\sqrt{\mu_0 \rho}$. This equation is identical to the circularly polarized Alfvén wave equation, except that $\boldsymbol{B}_1$ can be large but restricted to the sphere defined by $B_0$ and the Alfvén phase velocity $\boldsymbol{v}_a$ is precisely defined (not defined with time-averaged field).

This model leads to some important implications: (1) The spherically polarized Alfvén wave is an exact solution and is mathematically identical to the small-amplitude shear Alfvén mode; (2) If a radial jet is present in the system, i.e., $\boldsymbol{u}_{1r} \| \boldsymbol{B}_0$, in accordance with the observed "switchbacks," the spherically polarized Alfvén waves can only be outward-propagating. This is because to maintain the constant $B$ state, the only possible

polarization is $\boldsymbol{u}_1 = -\boldsymbol{B}_1/\sqrt{\mu_0\rho}$; 3. There exists a well-defined background field $\boldsymbol{B}_0$ for the constant $B$ state, and hence the constant magnetic magnitude $B$ can be regarded as a good proxy for the local $\boldsymbol{B}_0$, i.e., the local magnetic flux density.

In fact, the reversal of the magnetic field line (switchback) does not increase the number of field lines (thus field line density) and the Alfvén wave, being a solenoidal mode, does not change the local magnetic flux density. This establishes a connection between the magnetic magnitude (magnetic field line density) and the local magnetic flux density within the magnetically dominated coronal holes close to the Sun. The helioradial normalization of $B$ in the main text can therefore be regarded as mapping the magnetic flux density measured at different radial distances and longitudinal locations back to a cross section of the magnetic flux tube originating from the coronal hole.

## Appendix C
## PSP and Ulysses Data Analysis

The GSs in this Letter are compiled from the magnetic magnitude time series of PSP and Ulysses. The fluxgate magnetometer of PSP (S. D. Bale et al. 2016; T. A. Bowen et al. 2020) offers two versions of level-two data in RTN coordinates: mag_rtn_4_per_cyc and mag_rtn. The GS for intervals longer than one day are compiled with the low-resolution (4 samples per 0.874 s) data product and the rest are compiled with the high-resolution (256 samples per 0.874 s) mag_rtn. All magnetic magnitude data points for each interval are treated as independent samples drawn from a stochastic source and therefore the invalid (NaN) values are discarded and no interpolation is applied. The Ulysses magnetic field data is treated the same way.

## Appendix D
## Three-dimensional MHD Alfvénic Turbulence Simulation

The simulation is conducted using a 3D Fourier-transform-based pseudospectral MHD code (C. Shi et al. 2020, 2024a). The MHD equation set in conservation form is evolved with a third-order Runge–Kutta method. A detailed description of the simulation setup and normalization units can be found in (C. Shi et al. 2023). Here we briefly summarize the key parameters.

The domain of the simulation is a rectangular box with the length of each side being $L = 5$. The number of grid points along each dimension is 512. To ensure numerical stability, explicit resistivity and viscosity $\eta = \nu = 2 \times 10^{-5}$ are adopted besides a de-aliasing.

For the initial configuration, uniform density, magnetic field, and pressure are added: $\rho_0 = B = 1$, $P_0 = 0.1006$. The magnetic field has a small angle ($8.^\circ 1$) with respect to the $x$-axis, and it is inside the $x - y$ plane. On top of the background fields, we add correlated velocity and magnetic field fluctuations, i.e., the fluctuations are Alfvénic, with 3D isotropic power spectra. The reduced 1D spectra roughly follow $|k|^{-1.3}$. The strength of the fluctuations is $b_{\rm rms}/B \approx 0.14$ where $b_{\rm rms}$ is the rms of the magnetic field fluctuation.

## Appendix E
## Fluxgate Magnetometer Noise and Zeros Drift

There are several sources of error in the PSP fluxgate magnetometer measurements (S. D. Bale et al. 2016), including the instrumental noise as well as uncertainty in the zero offsets that drift in time (T. A. Bowen et al. 2020). The instrumental noise of each vector component is approximated as Gaussian white noise with a standard deviation $\sigma \simeq 0.05$ nT, and together produce a noise with a standard deviation of $\sigma_{\rm noise} \sim 0.1$ nT for the magnetic magnitude. $\sigma_{\rm noise}$ is usually much smaller than the standard deviation of the in situ measured $\sigma_B$ for all scales that we are interested in. Nevertheless, the GS of a ground-measured one-hour magnetic field time series for calibration is shown in Figure E1. The distribution of the noise signal is universally Gaussian regardless of scale and location, and the standard deviations are unanimously small. Therefore, most of the Gaussian structures we show in the Letter are real signals rather than instrument noise.

The error from drifting spacecraft offsets is a significantly larger contribution to the error as the approximated zero offsets drift over time and are calibrated each day (T. A. Bowen et al. 2020). The drift of the spacecraft offsets, which is thought to occur due to slowly varying currents on the spacecraft is not well constrained and varies over time. This error is not

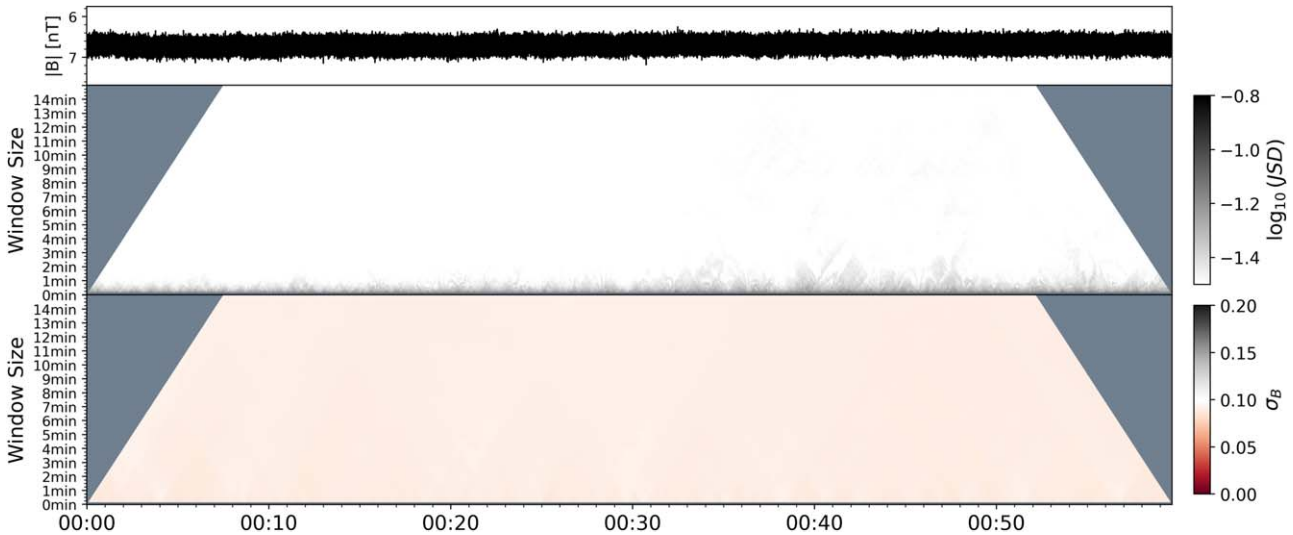



**Figure E1.** GS of the magnetic magnitude from the fluxgate magnetometer noise. From top to bottom: magnetic magnitude $B$ time series; GS of $B$; standard deviation scalogram of $B$.

Gaussian in nature but should introduce small offsets in the measured field from the real background magnetic field. Spacecraft rolls are used to determine zero offsets in both the inbound and outbound phases of each orbit and are updated daily by optimizing the measurements to ensure that spherically polarized magnetic field intervals maintain a constant magnitude. Typical offset values drift about 0.5 nT day$^{-1}$. Due to the continuous drift and non-Gaussian nature, the subday ($\lesssim$5 hr) structures are not strongly affected by the zeros drift. Days-long structures are also not affected because of the instrument calibration of the zeros offset.

## Appendix F
## Supplementary Materials

### *F.1. Supplementary Videos*

This manuscript contains one supplementary video: `gaussianity_skewness_scalogram_E12.mp4`.

It shows the GS and normalized standard deviation scalogram of magnetic magnitude with a window sized from 30 s to 15 minutes for the whole Parker Solar Probe E12. This video aims to show the self-similar magnetic structures revealed by GS and the corresponding substructures from the normalized standard deviation scalogram. For the first one minute, the GS looks different because of the low sampling rate of the fluxgate magnetometer. It also shows the skewness scalogram and normalized standard deviation scalogram of magnetic magnitude with a window sized from 1 s to 5 minutes for the whole Parker Solar Probe E12. This video aims to show the systematic tendency for magnetic holes in the magnetic magnitude distributions.

## ORCID iDs

Zesen Huang (黄泽森) https://orcid.org/0000-0001-9570-5975
Chen Shi (时辰) https://orcid.org/0000-0002-2582-7085
Marco Velli https://orcid.org/0000-0002-2381-3106
Nikos Sioulas https://orcid.org/0000-0002-1128-9685
Olga Panasenco https://orcid.org/0000-0002-4440-7166
Trevor Bowen https://orcid.org/0000-0002-4625-3332
Lorenzo Matteini https://orcid.org/0000-0002-6276-7771
Mingtao Xia (夏铭涛) https://orcid.org/0000-0002-2116-4712
Xiaofei Shi (石晓霏) https://orcid.org/0000-0003-3367-5074
Sheng Huang (黄胜) https://orcid.org/0000-0002-9951-8787
Jia Huang (黄佳) https://orcid.org/0000-0002-9954-4707
Lizet Casillas https://orcid.org/0000-0001-6248-183X

## References

Angelopoulos, V., Cruce, P., Drozdov, A., et al. 2019, SSRv, 215, 9
Aschwanden, M. 2011, Self-Organized Criticality in Astrophysics: The Statistics of Nonlinear Processes in the Universe (Berlin: Springer)
Aschwanden, M. J., Crosby, N. B., Dimitropoulou, M., et al. 2016, SSRv, 198, 47
Badman, S. T., Bale, S. D., Oliveros, J. C. M., et al. 2020, ApJS, 246, 23
Badman, S. T., Riley, P., Jones, S. I., et al. 2023, JGRA, 128, e2023JA031359
Bale, S. D., Badman, S. T., Bonnell, J. W., et al. 2019, Natur, 576, 237
Bale, S. D., Drake, J. F., McManus, M. D., et al. 2023, Natur, 618, 252
Bale, S. D., Goetz, K., Harvey, P. R., et al. 2016, SSRv, 204, 49
Bale, S. D., Horbury, T. S., Velli, M., et al. 2021, ApJ, 923, 174
Berger, T., Hillier, A., & Liu, W. 2017, ApJ, 850, 60
Bowen, T. A., Bale, S. D., Bonnell, J. W., et al. 2020, JGRA, 125, e2020JA027813
Chitta, L. P., Zhukov, A. N., Berghmans, D., et al. 2023, Sci, 381, 867
Davis, N., Chandran, B. D. G., Bowen, T. A., et al. 2023, ApJ, 950, 154
Del Zanna, L. 2001, GeoRL, 28, 2585
Erofeev, D. V. 2019, Ge&Ae, 59, 1081
Fargette, N., Lavraud, B., Rouillard, A. P., et al. 2021, ApJ, 919, 96
Fox, N. J., Velli, M. C., Bale, S. D., et al. 2016, SSRv, 204, 7
Harris, C. R., Millman, K. J., van der Walt, S. J., et al. 2020, Natur, 585, 357
Heinemann, M., & Olbert, S. 1980, JGRA, 85, 1311
Hollweg, J. V. 1973, JGR, 78, 3643
Hollweg, J. V. 1974, JGR, 79, 1539
Huang, Z., Shi, C., Sioulas, N., & Velli, M. 2022, ApJ, 935, 60
Johnston, Z., Squire, J., Mallet, A., & Meyrand, R. 2022, PhPl, 29, 072902
Kasper, J. C., Abiad, R., Austin, G., et al. 2016, SSRv, 204, 131
Kasper, J. C., Bale, S. D., Belcher, J. W., et al. 2019, Natur, 576, 228
Kasper, J. C., Klein, K. G., Lichko, E., et al. 2021, PhRvL, 127, 255101
Kruparova, O., Krupar, V., Szabo, A., Pulupa, M., & Bale, S. D. 2023, ApJ, 957, 13
Kullback, S., & Leibler, R. A. 1951, Ann. Math. Stat., 22, 79
Lam, S. K., Pitrou, A., & Seibert, S. 2015, Proc. of the Second Workshop on the LLVM Compiler Infrastructure in HPC (Austin Texas: ACM), 1
Lin, J. 1991, ITIT, 37, 145
Matteini, L., Horbury, T. S., Neugebauer, M., & Goldstein, B. E. 2014, GeoRL, 41, 259
Matteini, L., Horbury, T. S., Pantellini, F., Velli, M., & Schwartz, S. J. 2015, ApJ, 802, 11
Matteini, L., Tenerani, A., Landi, S., et al. 2024, PhPl, 31, 032901
McComas, D. J., Elliott, H. A., Schwadron, N. A., et al. 2003, GeoRL, 30, 1517
Moncuquet, M., Meyer-Vernet, N., Issautier, K., et al. 2020, ApJS, 246, 44
Müller, D., St., Cyr, O. C., Zouganelis, I., et al. 2020, A&A, 642, A1
Nielsen, F. 2019, Entrp, 21, 485
Panasenco, O., Velli, M., & D'Amicis, R. 2020, ApJS, 246, 54
Perez, J. C., Bourouaine, S., Chen, C. H. K., & Raouafi, N. E. 2021, A&A, 650, A22
Raouafi, N. E., Matteini, L., Squire, J., et al. 2023a, SSRv, 219, 8
Raouafi, N. E., Stenborg, G., Seaton, D. B., et al. 2023b, ApJ, 945, 28
Riley, P., Sonett, C. P., Tsurutani, B. T., et al. 1996, JGRA, 101, 19987
Shi, C., Panasenco, O., Velli, M., et al. 2022, ApJ, 934, 152
Shi, C., Sioulas, N., Huang, Z., et al. 2023, in AGU Fall Meeting 2023, held in San Francisco, CA, 11-15 December 2023, Session: SPA-Solar and Heliospheric Physics / Magnetic Structures and Waves in Solar Wind Turbulence II Oral (Washington, DC: AGU), SH51B–08
Shi, C., Velli, M., Tenerani, A., Rappazzo, F., & Réville, V. 2020, ApJ, 888, 68
Shi, C., Tenerani, A., Rappazzo, A.F., & Velli, M. 2024a, FrASS, 11, 1412905
Shi, C., Velli, M., Toth, G., et al. 2024b, ApJL, 964, L28
Squire, J., & Mallet, A. 2022, JPlPh, 88, 175880503
Tenerani, A., Velli, M., Matteini, L., et al. 2020, ApJS, 246, 32
Towns, J., Cockerill, T., Dahan, M., et al. 2014, CSE, 16, 62
Tsurutani, B. T., Ho, C. M., Smith, E. J., et al. 1994, GeoRL, 21, 2267
Uritsky, V. M., & Davila, J. M. 2012, ApJ, 748, 60
Vasquez, B. J., & Hollweg, J. V. 1996, JGRA, 101, 13527
Velli, M., Grappin, R., & Mangeney, A. 1991, GApFD, 62, 101
Virtanen, P., Gommers, R., Oliphant, T. E., et al. 2020, NatMe, 17, 261
Wang, X., He, J., Tu, C., et al. 2012, ApJ, 746, 147
Yu, L., Huang, S. Y., Yuan, Z. G., et al. 2021, ApJ, 908, 56
Yu, L., Huang, S. Y., Yuan, Z. G., et al. 2022, JGRA, 127, e2022JA030505